Econ. Environ. Geol.
Vol. 33, No. 1 p. 61-75, 2000.

Slip Movement Simulations of Major Fualts Under Very Low Strength

Moochoon Park* and Uk Han*

ABSTRACT: Through modeling fault networks using thin plate finite element technique in the San Andreas Fault system with slip rate over 1mm/year, as well as elevation, heat flow, earthquakes, geodetic data and crustal thickness, we compare the results with velocity boundary conditions of plate based on the NUVEL-1 plate model and the approximation of deformation in the Great Basin region. The frictional and dislocation creep constants of the crust are calculated to reproduce the observed variations in the maximum depth of seismicity which corresponds to the temperature ranging from 350°C to 410°C. The rheologic constants are defined by the coefficient of friction on faults, and the apparent activation energy for creep in the lower crust. Two parameters above represent systematic variations in three experiments. The pattern of model indicates that the friction coefficient of major faults is 0.17~0.25. We test whether the weakness of faults is uniform or proportional to net slip. The geologic data show a good agreement when fault weakness is a trend of an additional 30% slip dependent weakening of the San Andreas. The results of study suggest that all weakening is slip dependent. The best models can be explained by the available data with RMS mismatch of as little as 3 mm/year, so their predictions can be closely related with seismic hazard estimation, at least along faults where no data are available.

INTRODUCTION

Hubbert and Rubey (1959) debated over the strength or weakness of faults that is showing the impossible faults to explain large overthrusts with conventional theory. According to the previous studies, there are restriction in local solutions showing very low stress.

Bird (1978a) showed two oceanic subduction zones which have a mean shear stress of 20 MPa using force balancing calculations. A variant of this me- thod gave the same value for the thrust faults for- med during Indian Plate collision against the Eura- sian Plate (Bird, 1978b). Henyey (1968) searched unsuccessfully for a heat flow anomaly along the San Andreas fault (Fig. 1), however, he successfully suggested that its mean shear stress must be less than 20 MPa (Henyey and Wasserburg, 1971; Lachenbruch and Sass, 1980). Mount and Suppe (1987) compiled stress orientation data along the San Andreas fault and showed that the nearly orthogonal relation is required to obtain very low friction ($\mu \leq 0.1$). The result suggests that the standard model often predicts higher stresses by an order of magnitude.

It is important to decide whether these cases of low strength are local anomalies or regional representative. Furthermore, it would be helpful to determine faulting condition in as many tectonic settings as possible. For example, in thrusts, it is possible to explain that the low faulting strength can be caused by high pore pressure within the shear zone, as Hubbert and Rubey (1959) mentioned. In the case we might invoke low friction

Fig. 1. Location map of the study area.

* Department of Environmental Sciences, Korea Military Academy, Seoul 139-799, Korea

hydrated clays in fault gouge. We might be forced to consider unknown sources of pore pressure, or even to question the relevance of the friction law (Williams, 1995; Hickman *et al.*, 1995; Han and Keehm, 1997). In order to solve experimental problem, we tried to make three attempts to develop finite element codes that would permit computational trial with different hypothesized fault rheology. Every computed model has an assumed rheology and plate tectonic boundary conditions, and predict present surface velocity, strain rate, and stress. This paper aims that one will be to test whether its predictions of mean fault slip rates, stress directions and geodetic data are close to the reality.

THE RHEOLOGIC MODEL

In the rheological model, shear stress in the upper crust is given by the friction law:

$$|\sigma_s| \leq \mu(-\sigma_n - BP_p) + \sigma_c \quad (1)$$

where σ_s, σ_n and σ_c designate shear stress, normal stress and cohesion on the same plane, and is μ the coefficient of friction, B is the Biot coefficient (close to 1 in porous rocks), and P_p is the pore pressure. Usually, the pore pressure is assumed to be hydrostatic ($P_p=\rho_w gz'$, where ρ_w is water density, g is gravity, and z' is depth). For most rocks tested in the laboratory, the friction (μ) is approximately 0.85 (Brace and Kohlstedt, 1980; Han, 1991). This enables to predicted shear stress of 215 MPa on a purely strike slip fault about 15 km.

The base model is one in which the entire crust shares a common rheology, both in fault zones and in the blocks between. This common rheology includes both frictional and dislocation creep part, with the "brittleductile" transition between them depending upon temperature and strain rate. In the frictional part, the base coefficient of friction is 0.85, the Biot coefficient is 1, and the pore pressure (P_p) is assumed hydrostatic. For dislocation creep, we compute the shear stress σ_s from

$$\sigma_s = C[2\sqrt{II}]^{2/3} \exp(Q/(nRT))\dot{e}_s \quad (2)$$

where C is a constant parameter, II is the second invariant of the strain rate tensor, n is the stress exponent, Q is the molar activation energy, R is the gas constant, T is absolute temperature, and $\dot{e}_s$ is the shear strain rate. The creep activation energy Q varies from 100 to 400 kJ/m. This is approximated from experimental results using plausible lower crustal rocks (Kirby, 1983). For initial experimentation, the creep values were $C=1.9\times10^{8}P^{1/3}$ and Q=150 kJ/m; we will describe how better values were obtained empirically.

Each computed model induces results: long term average slip rates of faults, principal directions of stress, and relative velocities of geodetic benchmarks.

As for prediction of long term average slip rates, we used fault data with large offsets (>40 m on long faults, >5 m on short faults) in order to average several seismic cycles. Although late Quaternary rates are ideal, in many cases it was necessary to average as far back as the late Miocene in finding data. Most of the rate limits were already tabulated by Bird and Rosenstock (1984). Available data and data from northern California are listed in Table 1. Altogether, there are 79 rate limits that each model follows. The scalar measure of misfit that we adopted is the root mean square (RMS) prediction error, $\varepsilon_{geologic}$, in mm/year.

Directions of principal stresses were obtained from the compilation of Zoback and Zoback (1989). There are 221 stress data available in the region. Plots of this data show much local scatter which is not mechanically plausible, and may represent either technical problems or failure to average over sufficient depth. To quantify the model, we computed a variogram, which is a graph of the variance of the differences in stress orientation between all possible pairs of data versus the distance between them. From the value of linear variation diagram, we estimate whether the dataset contains errors with standard deviation of 17 degrees. Calculated relative velocities between pairs of points are not immediately comparable to geodetic results, because most geodetic data were obtained over short time periods during which there were no large earthquakes.

Thus, model velocities are discontinuous across faults, while most geodetic profiles are continuous. We must correct the one after the other before comparison; we correct the model predictions for more complete knowledge of the model than of the reality. In each fault element, we modify the

Table 1. Geologic slip rate.

Fault	Slip*	Rate (mm/year)	References
Calaveras	RL	3±?	Sarma-Wojcicki *et al.* (1986)
Coast Ranges	RL	20±?	Paul Segall (1995)
E. CA shear zone	RL	6-12	Dokka and Travis (1990a)
W. Great Valley	RL	31±1	Paul Segall (1995)
Hayward	RL	7-10	Lienkaemper *et al.* (1989)
Panamint Valley	RL	1.6-3.2	Zhang *et al.* (1990)
Panamint Valley	RV	≤4.7	Zhang *et al.* (1990)
Rodgers Creek	RL	≥2.1	Budding *et al.* (1991)
N. San Andreas	RL	10-30	Cummings (1968)
N. San Andreas	RL	3.75±?	Sarna-Wohcicki *et al.* (1986)
N. San Andreas	RL	≤25	Prentice (1989)
N. San Andreas	RL	≥7.5	Ward and Page (1989)
N. San Andreas	RL	39±3	Paul Segall (1995)
S. San Andreas	RL	13-28	Prentice *et al.* (1986)
S. San Andreas	RL	14-25	Yeats and Matti (1989)
San Cayetano	RV	5.2-13.8	Harden and Huftile (1990)
San Jacinto	RL	13.3-24	Morton *et al.* (1986)
San Jacinto	RL	6-14	Prenrice *et al.* (1986)
San Jacinto	RL	≥7	Rockwell *et al.*(1990)
San Jacinto	RL	≥1.7	Wesnousky *et al.*(1991)
Santa Cruz Island	RV	1.27-2.5	Pinter and Sorlien(1991)

*Slip component directions: RL=right-lateral; RV=relative vertical (which is less than true dip-ship)

long term average solution by adding rectangular patch dislocations extending from the surface down to the brittle and ductile transition on the model. We take the rate of slip on these dislocation patches to be the opposite of the model long term average slip rate, so that the fault becomes temporarily locked in the upper crust. Then, the sum of the far field elastic displacements from these dislocations (Mansinha and Smylie, 1971) is a vector field of velocity corrections due to temporary fault locking. This vector field is added to the original long term average velocity predictions before scoring the model.

For simplicity, and to avoid any problem associated with an arbitrary choice of a reference frame, we compare geodetic data with corrected predictions in the secular rates along baselines. We use two complementary data sets of baseline rates. From the U.S. Geological Survey Reports (Michael Lisowski, personal communication, 1992), we obtained 796 baseline rates along laser geodimeter lines in networks lying along the San Andreas fault system. Most of these data were graphically presented in Savage *et al.* (1990) and Lisowski *et al.* (1991). The laser geodimeter data had been processed to remove coseismic slips before the determination of rates. Both rate datasets contained estimated rate errors, which we used as weights in calculating weighted RMS prediction errors as the scalar norms of the misfit of our models, ε_{VLBI} and ε_{laser}, in mm/year.

Because these three datasets may not always point to the same conclusion, we also created a scalar measure of global mismatch, ε_{global} (in mm/year), by combining the three individual error measures. The formula of study, which is designed to give equal weight to geologic, geodetic, and stress data, is:

$$\varepsilon_{global} = 1/3[\varepsilon_{geologic} + (\varepsilon_{VLBI} + \varepsilon_{laser})/2 + (\varepsilon_{stress} - 17^{\circ})/2^{\circ}] \quad (3)$$

FINITE ELEMENT TECHNIQUES

The computed codes based on assumptions and approximations are as follows;

1. Flat earth. For simplicity and speed of execution, our models are created in a Cartesian coordinate system attached to a nominally flat Earth, with unidirectional gravity along x_3 (or z) direction.

2. Creeping flow. We neglect all insignificant acceleration in comparison with gravity. We will instead attempt to compute the long term average stress and average slip rate of each fault.

3. Inelastic deformation. Our finite element models neglect elastic strain. This enables our code to be structured differently from nonlinear viscoelastic codes. However, when such codes approach a quasi steady state under constant velocity boundary conditions, it is typically found that the elasticity is not important in the viscoelastic solutions, and was only a means to an end.

4. Constant phase. No metamorphic or melting processes are considered.

5. Incompressibility. Neglecting the elastic strain, we treat the volumes and densities of rocks constant except when applying short term elastic corrections.

6. Constant thermal properties. We assume constant thermal conductivity and radioactive heat

production in all parts of the crust.

7. Steady state, vertical heat conduction. The geotherms computed beneath each surface point are assumed to depend strictly on local heat flow and the regional thermal constants.

8. Inelastic rheology. All rocks are assumed to deform either by frictional sliding on fault surfaces, or by nonlinear dislocation creep. The selection is made by evaluating the shear stress required under each mechanism at the current strain rate, temperature, and stress, and selecting the lower value. There is no cohesion.

9. Fictitious viscous compliance. All finite element codes lead to linear systems, which become ill-conditioned if their coefficient matrices have excessively large condition numbers. To prevent this, we restrict the shear stress at all points not to exceed the product of strain rate and an artificial uniform viscosity. This viscosity is then set high enough that fictitious viscous compliance has little effect on the solutions.

10. Lithostatic vertical stress and isostasy. We neglect any horizontal gradients of the vertical integrals of vertical tractions on vertical planes. We approximate the vertical normal stress σ_{zz} as lithostatic at all points. The vertical traction on the base of the crust is computed to support the topography, allowing for the local density structure of the crust.

11. Vertical integration of stresses. We use "thin plate" models, in which the horizontal components of the force balance are vertically integrated through the crust. As a consequence, stress output is naturally expressed in terms of vertical integrals.

The first set of models in this series was presented by Bird and Baumgardner (1984). In their study only the San Andreas fault was represented, and this was done very crudely with a thin belt of weaker faults. The models were compared to three very preliminary data sets which represent historical seismic moment distribution, direction of shortening (or stress), and rates of vertical movements. The best model found was one in which the shear stress of San Andreas fault material was 12% of the strength of surrounding crust at equal temperature and strain rate. Also unacceptable slumping was predicted if the assumed strength of unfaulted crust was reduced more than 50%.

In the second effort, we incorporate mantle drag by assuming various patterns of the horizontal velocity field on the top of the mantle. These assumed flows were linked to the surface velocity solutions by the dislocation creep rheology which is assumed for the lower crust. Additionally, the studies introduced a fault element for thin plate models, in which any orthogonal component of the horizontal projection of fault slip is assumed to result from dip slip, and the shear traction on the fault plane is required to be parallel with the slip vector.

The finite element grids are composed of two types of elements: isoparametric triangular continuum elements, and isoparametric curvilinear fault elements.

Positions along the trace of the fault, within any one element, are defined using an internal variable s, which varies from 0 at the node-1,6 end to 1 at the node-3,4 end. Internal coordinate positions are related to external coordinate positions by a superposition of the 6 nodal functions f_i (s):

$$x(s)=\sum_{i=1,3} x_i f_i(s)=-\sum_{i=4,6} x_i f_i(s) \qquad (4)$$

$$y(s)=\sum_{i=1,3} y_i f_i(s)=-\sum_{i=4,6} y_i f_i(s)$$

where i refers to the local node numbers (1-6), x_i and y_i are the external coordinate of the 6 nodes.

The dip angle θ is not defined quite as in geology; it is measured from horizontal on the node 2 side, so in any fault element where the hanging wall is on the node 5 side, the dip will be greater than $\pi/2$. Dip at any internal point is determined from the same kind of superposition of nodal functions, using data values θ_i at nodes 1-3:

$$\theta(s)=\sum_{i=1,3} \theta_i f_i(s) \qquad (5)$$

The same method is used to interpolate other necessary parameters, such as crustal thickness, heat flow, and topography. Because of the way the nodal functions are defined, the horizontal components of the fault slip are easily obtained from:

$$\Delta V_x(s)=\sum_{i=1,6} (V_x)_i f_i(s) \qquad (6)$$

$$\Delta V_y(s)=\sum_{i=1,6} (V_y)_i f_i(s)$$

where V_x is the x component of velocity and $(V_x)_i$ is the V_x value at node i (local numbering), and Δ refers to the motion of the node 1-3 side with respect to the node 4-6 side.

The experiment will evaluate the frictional traction on the shallow parts of the fault element, based on the Mohr Coulomb Navier friction law of equation. We will assume that the vertical stress σ_{zz} is lithostatic, the pore pressure P_p is hydrostatic, and the Biot coefficient B is spatially uniform. Under this law the lithostatic deviatoric stress tensor is proportional to depth. Lithostatic deviatoric stress $\Delta\sigma^L_{ij}$ is defined as:

$$\Delta\sigma^L_{ij}=\sigma_{ij}-\sigma_{zz}I_{ij} \quad (7)$$

A second constraint is that the shear traction on the fault plane must be parallel to the slip rate vector. It follows geometrically that the lithostatic deviatoric normal stress on the fault, at unit depth, is:

$$\Delta\sigma^{L*}_n=\tan\theta \sin\Psi T^*_s \quad (8)$$

where T_s^* is the unknown shear traction on the fault at unit depth, and Ψ is the rake angle of fault plane. According to friction theory, the second equation relating $\Delta\sigma^L_{ij}$ and T_s^* is:

$$T^*_s=\mu(-\sigma^*_{zz}-\Delta\sigma^{L*}_n-BP^*_p) \quad (9)$$

We adopt the weak fault model of Turcotte *et al.* (1980) in which 90% of the shear falls within a zone whose full width can be described by W (the width of the shear zone):

$$W=z'/2 \quad ; \ 'z\leq 17km \quad (10)$$

$$25-2.83z'+0.11z'^2 \quad ; \ 'z>17km$$

After the brittle and ductile zones are located, it is useful to compute (by numerical integration) the ratio of the integral of the shear traction down the fault dip to the slip velocity. This will be referred to as τ:

$$\tau\equiv\left\{\int \inf(T_s^{fricrion},T_s^{creep})d\beta\right\}/\sqrt{(\Delta V_\alpha^2+\Delta V^2)} \quad (11)$$

where $\Delta V_\beta, \Delta V_\alpha$ is the motion of velocity which $+\beta$ (perpendicular to the $+\alpha$), $+\alpha$ (parallel to the fault strike) are toward to the fault.

In this study, 56 geologic estimates of long term fault slip rates are used for modeling. The best models were achieved when the mantle drag was convergent on the Transverse Ranges, and a low friction is set to the San Andreas Fault ($\mu = 0.3$).

In most cases, faults were forced to connect with other faults, even where the actual intersection is obscured by Quaternary sediments. It is important to figure out the locations of fault if the intention is to perform numerical experiments with faults much weaker than intervening blocks.

The dip values that we assigned to most faults were either 90° for strike slip faults, 65° for normal faults, or 25° for thrust faults. These values should be corrected if the faults are initiated following the friction law (Equation 1), in rocks with a "standard" friction coefficient of 0.85. Presumably, any lower friction developed later during gouge formation, weathering, and/or infiltration by fluids. The dip of the Loma Prieta segment of the San Andreas was assigned to 70°, according to the 1989 aftershock distribution.

To approximately represent the three dimensional structure of California, each node of the grid was assigned values of elevation, heat flow, and crustal thickness; at other point, these values were interpolated using the quadratic nodal functions. Crustal thickness is actually quite controversial, and we selected the map of Mooney and Weaver (1989) partly because of its simplicity and lack of short wavelength features which (if incorrect) might bias the behavior of particular faults. The heat flow distribution which we assumed is shown in Fig. 2; it was hand contoured from references listed in Bird and Baumgardner (1984), plus northern California values obtained from Lachenbruch and Sass (1980). In the Ventura Basin area, we adopted the argument of De Rito *et al.* (1989) that through most of the crust the heat flow is higher than the surface value.

For simplicity, we assigned uniform intensive properties to the whole crust. The rock density (ρ) is 2800 kg/m^3, and the density of pore fluids (ρ_p) is 1000 kg/m^3. The volumetric thermal expansion coefficient (α) is $3\times10^{-5o}K^{-1}$. The thermal conductivity (k) is 3.0 $Wm^{-1o}K^{-1}$. The radioactive heat production (A) is 0.3 μWm^{-3}. To evaluate these values, we computed model temperatures on the Moho, and found a good correspondence between model Moho temperatures over 900°C and volcanic areas.

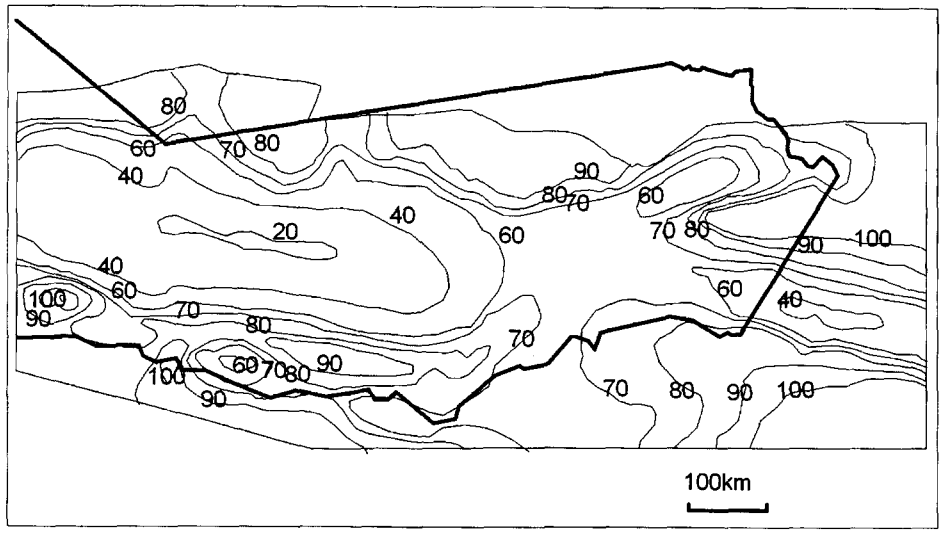

Fig. 2. Heat flow distribution used in the calculations. Great Valley and Peninsular Ranges show low value, Coast Ranges, Basin & Ranges province and Salton trough show high value. High heat flow region is weaker, as strength is inversely is inversely proportional to the square of heat flow.

The boundary conditions on the sides of the model are either prescribed velocity or (deviatoric) traction free. All along the southwest side, we impose the Pacific plate velocity from the NU VEL-1 model of DeMets *et al.* (1990). Along the Northeast side, we adopt a simple model of Basin and Range extension in which the strain rate is uniform 34° and 41° N, direction and the along extension direction N56° W. The integrated strain rate is 10 mm/year. Most nodes on the southeast and northwest margins are left free, so as not to impose slip on any particular fault. However, the experiment shows that for reasonable results it is necessary to limit the northwestward velocity of the large rigid Sierra Nevada or Great Valley block. We do this by limiting the velocity component along N56° W to 10 mm/year at a single node along the northwestern margin. This has disadvantage of creating a local stress singularity, but the advantage of not imposing any particular rotation or NE-SW velocity on this large block.

In this study, we correct the two technical problems compared with previous work and take advantage of faster computers to present three set of experiments totaling 155 models, all of which are fully converged. We also use two new datasets of stress direction and geodetic in addition to geologic slip rates for objective scoring of the quality of these models. Finally, we present tests of a third fault flow law parameter, a possible weakening proportional to net slip, in addition to those parameters previously considered.

COMPUTATIONAL EXPERIMENTS

In the first set of models, the base of the crust was free from shear tractions. The friction coefficient of all fault elements was reduced in nine steps from 0.85 to 0.085, with all other parameters held fixed. Subjectively, this reduction in friction caused a huge improvement in the realism of the output. In the model with fault friction 0.85, all faults were locked except the Elsinore and the central California segment of the San Andreas; these are nearly aligned with relative plate motion. The many faults trends are not predicted by elementary friction theory only became active very gradually as the friction was reduced. The geologic and stress data confirm our subjective impression by showing minimum error at fault friction of 0.17. The two types of geodetic data seem to have no ability to discriminate, and fit all models well with 3 mm/year error. This is apparent because the velocity field of elastic strain around a

set of temporarily locked faults is similar to the velocity field of permanent inelastic strain around a set of permanently locked faults.

Before conducting further experiments on fault friction, we used the best model from group as a tool to experiment with the dislocation creep law of the lower crust. Our goal was to obtain a relationship between its two unknown parameters (C and Q) by matching the observed depth of the brittle and ductile transition in California, San Andreas tectonics.

There have been a number of publications presenting accurate hypocenters on particular fault segments in Table 2. In each case, we picked an estimated depth of deepest real seismicity by using the shoulder of the frequency and depth distribution to allow for event mislocations. Then, we compared these depths with the local heat flow, estimated from Fig. 2. Fig. 3 shows a definite suggestion of an inverse relationship, as we would expect if the brittle and ductile transition fell on an isotherm. If model thermal parameters are correct, then the best fitting isotherm temperature would be 410°C. In theory, the transition should not fall exactly on an isotherm because different faults have different strain rates, and because thrust faults have higher stresses than most strike slip faults. Thus, our next step was to adjust the C and Q creep parameters of our model keeping fault friction at 0.17 until the RMS error in predicted transition depth was minimized. We found that the models which best fit this criterion had

$$C = De^{-2.80\times10-5\,Q} \qquad (12)$$

for C in $P^{1/3}$, Q (creep activation energy) in J/m and D is $e^{12.2}$. This implies a mean transition temperature of 350°C which should be more accurate than the 410°C mentioned above, because it comes from a much more sophisticated model. On the laboratory rheologies cited by Kirby (1983), this line passes closest to those of Westerly granite (on the low Q end), aplite, albite rock, and anorthosite (on the high Q end), but our rheology is much weaker than the laws reported for diabase, quartz diorite, and clinopyroxenite.

In the second set of models, group, we used this relationship to vary C and Q together without violating the seismic constraint. The importance of varying Q is that it determines the extent of coupling between the upper crust and the upper mantle across the lower crustal shear zone. If the shear stresses at the brittle or ductile transition are fixed, a low value of Q means that a base of the crust is almost as strong, and the coupling to the upper is firm. Conversely, a high value of Q means that

Table 2. Depths to brittle-ductile transition.

Fault/area	Heat Flow (mW/m^2)	Deepest Events	410°C Depth	Model* 1991-12
San Jacinto	61	19	17.5	20.9
Elsinore	65	21	16.3	19.1
San Jacinto	67	17	15.8	18.0
Banning	67	20	15.8	16.5
W. Trans. Ranges	69	15	15.3	16.0
San Andreas (Central Area)	73	12	14.3	15.9
San Andreas (Basin and Range)	74	14	14.1	17.2
San Jacinto	78	13	13.3	16.9
San Andreas (Coastal Ranges)	80	10	13.0	15.6
Hayward	83	11	12.5	15.8
N. San Andreas	86	12	12.0	15.6
Rodgers Creek	90	12	11.4	13.2
N. San Andreas	94	13	10.9	12.4
Coso Range	96	9	10.7	13.0
Imperial Valley	130	12	7.8	11.2
Geysers	130	4	7.8	9.0

*Data sets adopted from Bird (1989) as a result of experiments

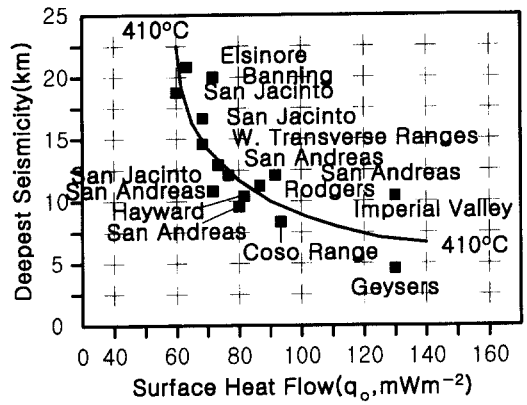

Fig. 3. Maximum earthquake depth versus surface heat flow (from Fig. 2) for regions in California. There is a suggestion of an inverse relationship, which would be expected if the brittle and ductile transition fell on an isotherm. Curve shows model depth of 410°C isotherm, based on assumed thermal conductivity of 3.0 $Wm^{-1}\,°K^{-1}$.

there are decades of strength decrease between mid crust and Moho, and the upper crust is essentially decoupled.

In all of the following models, we assumed a common pattern for the horizontal velocity field of the Moho. This was pattern suggested by Bird (1989), Bird and Baumgardner (1984). They have developed models to solve some relations about the "mantle San Andreas" at the Transverse ranges, with downwelling occurring from the west end of the Santa Monica Mountains to the east end of the San Bernadino Mountains. One important exception was that we only prescribed the Moho velocity at west of the "mantle San Andreas" (where there is Pacific plate lithosphere) and at east of the central Mojave Desert (where there is North American plate lithosphere). The remaining area is covered by the huge Sierra Nevada or Great Valley block, and there is so low heatflow that any Moho velocity we imposed would be directly transferred to the surface; this seemed mechanically unreasonable because the upper mantle is not part of large plate like the Pacific or North American.

We wished to see if the conclusion of low friction value is robust when the possibility of crust or mantle coupling is considered. That is, the strange pattern of southern California faults might be due to mantle drag rather than to inherited weakness? In model group, we used 81 calculations to test 9 different values of fault friction together with 9 different values of Q. The high Q models of this group are almost identical to those of group I, while the low Q models have increasingly large amounts of mantle drag. For example, in the Q= 100 kJ/m models, the Moho tractions around the Transverse Ranges are mostly 8~14 MPa.

As shown in Fig. 4, mantle drag does improve the models, but it does not eliminate the need for low fault friction value. As before, the geologic and stress data give the clearest indications. Geo-

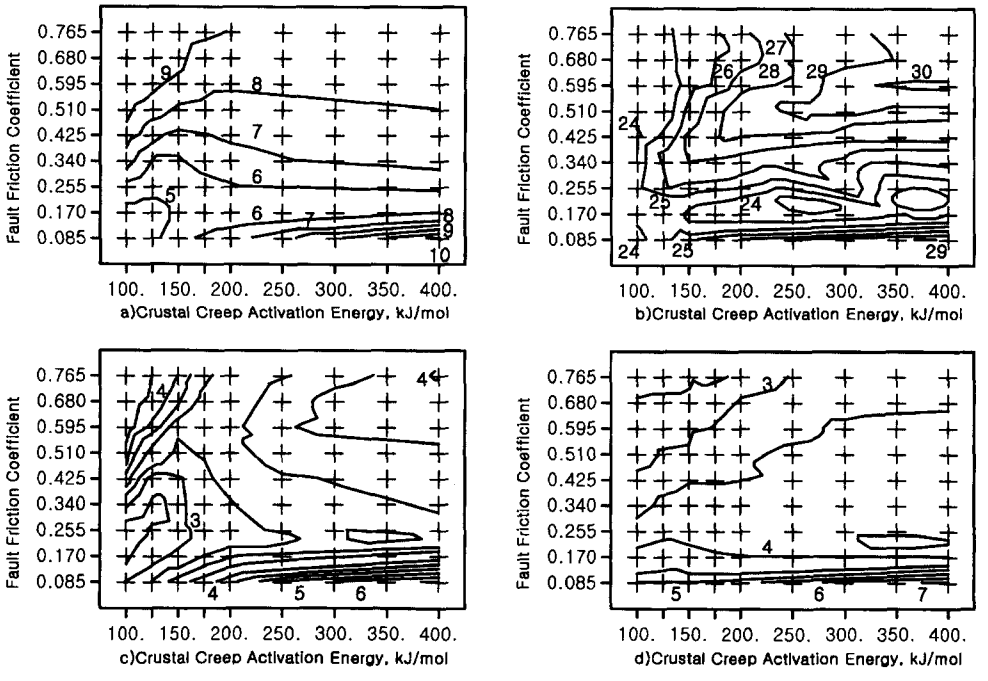

Fig. 4. Calculated prediction errors for the model. a) Geologic (fault) slip rate RMS prediction errors. There is a clear prefernce for fault friction coefficient of 0.255 or less. Low crustal creep activation energies are also favored. Contour intervals are 1.0 mm/year. b) Most compressive stress direction (weigted mean errors). At least, 17° of RMS error is due to problems in the dataset. Fault friction coefficients of 0.17~0.255 are preferred. Contour intervals are 1.0 degree), c) VLBI Baseline rate (weighted RMS prediction errors). Using this data alone, the very weakest faults in friction of 0.085 could be rehected. Contour intervals are 0.25 mm/year. d) Geodimeter baseline rate (weighted RMS prediction errors). This is the dataset which shows a preference for strong faults, Contour intervals art 0.5 mm/year.

logic data in Fig. 4(a) show a preference for fault friction of 0.255-0.17, and as mantle drag is increased this optimum friction may actually decrease; it certainly does not rise. Mantle drag slightly improves the quality of weak fault models, but has the opposite effect on strong fault models.

The stress data in Fig. 4(b) also show a preference for fault friction of 0.255~0.17, and the minimum error now found is about 17° in the data. Stress data also show a preference for strong mantle drag in the strong fault models, but not in the weak fault models. The geodetic data are less useful. The primary conclusion from VLBI data in Fig. 4 (c) and laser data in Fig. 4 (d) is that the lowest fault friction value of 0.085 can be rejected. Aside from this, the range of misfit variation is only about 1 mm/year. Furthermore, the two data types suggest different conclusions: VLBI alone confirms the weak fault, strong drag corner of parameter space already identified from geologic and stress data; laser data is best fit by strong fault models. When these scores are combined according to our formula for ε_{global}, the net result is that scores are best fit at the fault friction coefficient of 0.255~0.17, independent of the level of mantle drag. This shows that the conclusion of low friction value is robust with respect to possible mantle forcing of the surface velocity field.

Although this conclusion seems firm, it is not quite intellectually satisfying. Many authors have pointed out that fault networks have a fractal character, and that in fact all outcrops are faulted on some scale. We have made a binary division between "large" faults which are weak and crustal blocks containing "small" faults, which are strong; yet in nature there is likely to be some transition between these. If we know the reason and mechanism of this transition, it might well imply that there should be strength variations among the faults already included in our grid.

The one hypothesis of this kind that we have tested is that, "Effective fault friction decreases linearly with increasing net slip, independent to the strain rate". Also there is objective geologic data on the net slip of most faults in Table 3 which may be used in testing the hypothesis.

This hypothesis also has an underlying mecha0 nical model, although it very speculative. Byerlee (1990) has pointed out that fault gouge has non-Darcy hydrology below a threshold pressure gradient, at which the water forms a gel in fine pores. Thus, fault gouge may sustain anomalous pore pressure for very long times between earthquakes. Rice (1990) has argued that there is a source of pore water at near lithostatic pressure in the lower crust or mantle, and that it rises preferentially along faults. Assuming a constant threshold pressure gradient for all gouge, this fault can sustain a higher pore pressure anomaly at the center if there is a source of pressurized fluids. If the fault obeys friction theory and continues to have an intrinsic friction of 0.85, it will be greatly weakened by this P_p term. According to this theory, the amount of anomalous weakness should be proportional to net slip until it reaches some poorly understood asymptotic limit.

We have tested this hypothesis in model group III, which is comprised of 64 models. We formed all possible combinations among intrinsic fault friction (IFF) of 0.68, 0.51, 0.34, 0.17, slip dependent weakening (SDW) on the San Andreas of 0%, 30%, 60%, 90%, and crustal creep activation energy (Q) of 100, 150, 200, 300 kJ/m. Faults other than the San Andreas had a smaller slip dependent weakening in proportion to their estimated slip from Table 3.

The geologic data are invariably better fit by models with slip dependent weakening; the improvement is greatest at 30%, and less at 60% or 90%. The strong preference for low friction on all faults is unchanged. The best fit is at IFF 0.17, SDW 30%, Q 100, with RMS mismatch of 3.9 mm/year.

The stress data always fit better when slip dependent weakening is included. By this measure, the improvement is continuous, and the best model is IFF 0.34~0.68, SDW 90%, Q 100 where the error is reduced to 19°. Thus, unlike the geologic data, the stress data alone fit well by a model in which only the San Andreas fault zone is extremely weak, while "smaller" faults of less slip may have intrinsic friction only slightly less than the surrounding blocks. To explain this, it should be remembered that the locations at which the stress data were collected are strongly concentrated around the San Andreas.

The model best fitting the VLBI data compared to 2.6 mm/year RMS is the same as the best geologic model (IFF 0.17, SDW 30%, Q 100), but the

Table 3. Assumed net slips of the san andreas tectonics.

Fault	Net Slip (KM)	References
North San Andreas	295	Dickinson *et al.* (1972)
Sorth San Andreas	225	Ehlert and Ehlig (1977)
San Gregorio-Hosgri	115	Graham and Dickinson (1978)
Garlock	64	Davis and Burchfiel(1973)
Hayward-Rodgers Crk	44	Sarna-Wojcicki (1986)
Elsinoire-Whitter	40	Crowell and Syvester (1979)
Morales	25	Segall P. (1995)
San Jacinto	24	Sharp (1967)
Calaveras-Sunol	23	Sarna-Wojcicki (1986)
Agua Blanca	15	Allen *et al.* (1960)
Calico	9	Dokka (1983)
Hunter Mountain	9	Burchfiel *et al.* (1987)
Santa Monica	8	Lamar (1961)
Rose canyon	4	Kennedy (1975)
Newport-Inglewood	3	Yeats (1973)
Camp Rock	3	Dokka (1983)
Santa Suanna	3	Barnhart and Slosson (1973)
Palos Verdes	2	Yeats *et al.* (1990)
W. Great Valley	2	Segall P. (1995)

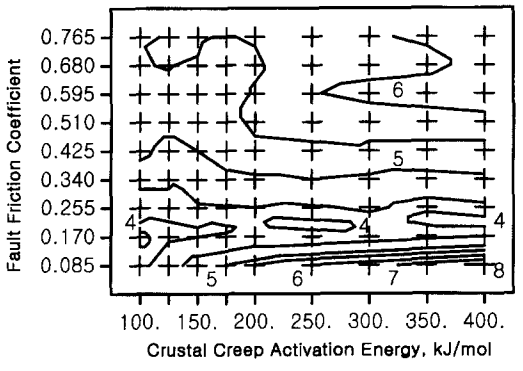

Fig. 5. Combined prediction errors. The primary result is that fault friction of 0.17~0.255 is preferred Low activation energies implying stronger mantle drag are also preferred. Contour intervals are 0.5 mm/year.

minimum in mismatch is extremely broad. The result from this dataset is a contradiction of the preference for large SDW displayed by the stress data; VLBI prediction errors rise by almost 2 mm/year as SDW increase from 30% to 90%.

The laser geodimeter data agree with geologic and VLBI data in preferring a SDW of 30% to higher or lower values. However, as before, this dataset also shows a weak preference for uniformly high fault friction; the best result is at IFF 0.68, SDW 30%, Q 150 which fits to 2.0 mm/year. The reasons behind this are obscure; that model has almost no fault slip and is clearly unacceptable for explaining either the geology or the seismicity of California.

In the overall best model (IFF 0.17, SDW 30%, Q 100), all faults are weak, but the San Andreas is slightly weaker. However, the minimum of mismatch is broad, and there is a tradeoff between IFF and SDW such that the scores are respectable as long as the San Andreas fault is weak. For example, if one prefers a model (IFF 0.68, SDW 90 %, Q 100) because of its stronger theoretical basis, thepenalty in terms of increased mismatch is only 0.7 mm/year. Details of the overall best model are given in Fig. 6 (slip rates), 7 (stresses) and Table 4.

These models are most useful in suggesting estimates for offshore and coastal faults which are difficult to access, for thrust faults which typically 'bury their evidence', and for faults in less populous areas which have been given low priority in funding of studies. For example, these models address the controversy over the Hosgri fault, where Hamilton and Willingham (1977) inferred only 2-4 mm/year from geologic evidence. We never find rates over 3 mm/year on the San Gregorio-Carmel Canyon-Hosgri system in our models, so the lower rate is probably appropriate for seismic hazard evaluation with regardless of which is the correct mean rate for Pliocene Quaternary time.

In the southern California borderland, we confirm that the shoreline cutting Newport-Inglewood-Rose Canyon-Vallecitos and Palos-Verdes-Coronado Bank systems are moving at no more than a few millimeters per year. One surprising result here is that we have good models in which the slip on the outer Santa Barbara Island-San Diego Trough-Agua Balanca system increases northwestward, from about 2 mm/year in Baja California to as much as 19 mm/year at the intersection with the San Barbara Channel structures.

It is important to estimate the slip rates of the thrust faults along the southern margin of the Transverse Ranges because of the high population densities there. Geodetic data are still inconclusive, and geologic rates must usually be treated as lower limits because of the tendency of thrusts to spray over a broad zone. Thus, it was ominous when Bird and Rosenstock (1984) used rigid block kinematics to infer slip rates of 7~15 mm/year along

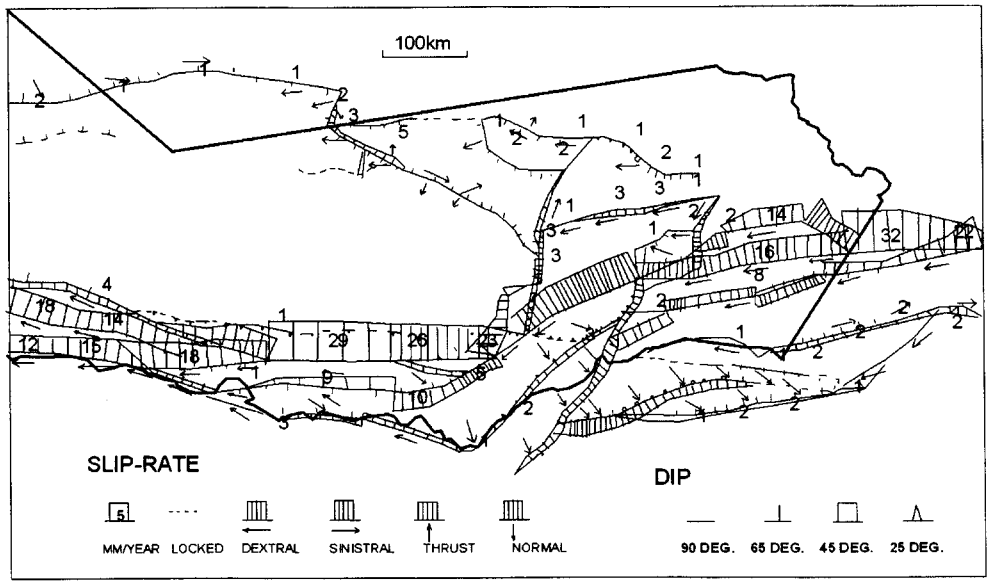

Fig. 6. Fault-ship (displacement vector) rate predictions of the most successful model. All rate are in mm/year, and represent the average over several seismic cycles. The relative slip direction of the hanging wall is shown by unit vector. Dashed faults had slip rates very low under 0.5 mm/year. These may be useful for seismic harzard evaluation.

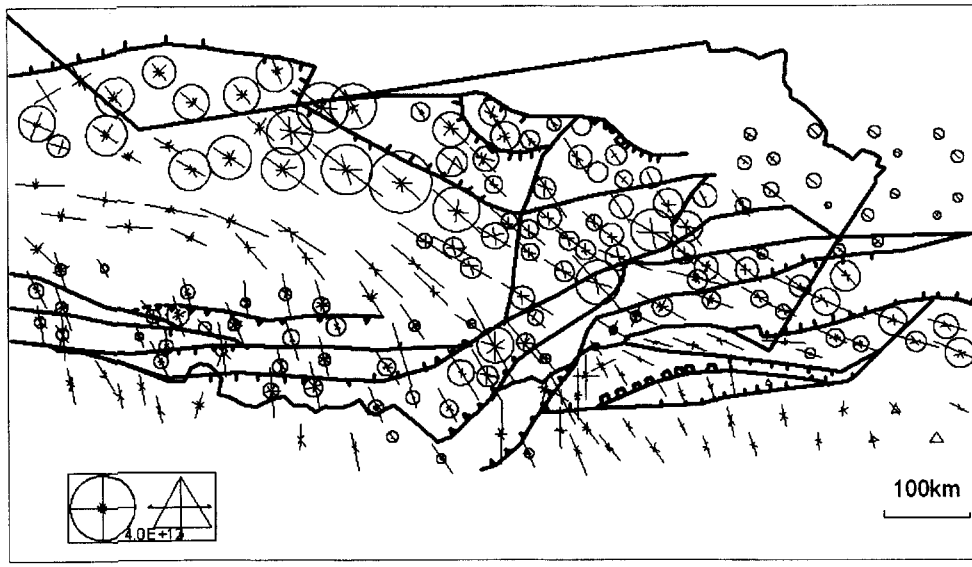

Fig. 7. Vertically integrated standardized deviatoric stress predictions of the most successful model. Vectors show the vertical integrals of the deviatoric principal horizontal stresses. Circles are used to show the vertical integral of standardized deviatoric vertical compression. Contour and shading refer to the vertical integral of the greatest shear stress. Note the focusing of horizontal compression into the strong Sierra, Great Valley and Peninsular Ranges blocks, and a rotation toward the normal og the San Andreas fault in northeun Califonia.

this zone. Weldon and Humphreys (1986) showed an alternative kinematic model with slower thrusting, but did not resolve the new problems that this would create in the borderland. In this study, we find rates that are about half as great as Bird and Rosenstock's (1984), but still indicative of real

Table 4. Results of slip rate estimates for major faults.

Fault	Geologic Rate	Geodetic Rate	Good Models	Best Model	Our Conclusion
Agua Blanca	2.4~5.0	·	0.2~1.3	0.7	≦2.4
Banning	≥1.7	·	0~0.3	0.2	≦1.7
Elsinore	0.8~0.9	8.0~16.0	0.4~18.0	7.5	8.0~9.0
Garlock (Mohave)		·	0.3~9.9	2.8	0.3*~9.9*
Hayward	7.0~10.0	·	1.0~22.0	14.7	7.0~10.0
Hogri	2.0~19.0	·	0.2~3.1	2.1	2.0~3.1*
central Mojave group	6.0~12.0	5.4~10.0	0.1~3.4	2.8	6.0~10.0
Newport-Inglewood	0.4~0.8	·	0~0.2	0.0	≦0.4
Rodgers Creek	≥2.1	·	0≥2.40	14.4	2.1≥22.0
San Andreas (Mecca)	21.035.0	18.0~22.0	3.5~38.0	14.1	21.0~22.0
San Andreas (San Gorgonio)	13.0~28.0	12.0~20.0	0.4~36.0	4.4	13.0~20.0
San Andreas (San Bernardino)	≤29.0	·	5.6~39.0	11.1	5.6*~29.0
San Andreas (Pearblossom)	35.0~60.0	18.0~30.0	16.0~33.0	22.0	18.0~30.0
San Andreas (San Francisco)	10.0~38.0	16.0~24.0	8.3~46.0	18.1	16.0~24.0
San Andreas (Tomales Bay)	≤25.0	·	5.2~38.0	15.1	5.2*~25.0
San Jacinto	13.3~14.0	11.0~15.0	0.2~30.0	16.2	13.3~14.0
Santa Monica	0.8~1.1	·	0.3~18.0	10.8	0.8~1.1
Sierra Nevada	0.3~1.5	·	0.1~6.9	0.9	0.3~1.5

*marks conclusions which depend on computer models, all figures in mm/year

hazard.

The Cucamonga fault slips at about 7 mm/year and the Sierra Madre fault rate is 3~6 mm/year. Along the southwest branch of this system of Santa Monica and Malibu Coast faults, the model rates are scattered, from under 1 to over 18 mm/year; however, since there is a geologic constraint showing slow motion (≤1.1 mm/year) on the Santa Monica fault, this probably applies to the whole branch. On the northwest branch (Sierra Madre-San Fernando-Santa SusannaSan Cayetano-Red Mountain-Santa Barbara Channel faults) the models suggest an upper limit of 7 mm/year for the San Fernando fault and an upper limit of 3 mm/year for the Santa Barbara Channel fault. The fact that the fastest-slipping models just match the lower geologic rate limit (9 mm/year) on the central Red Mountain-San Cayetano fault segment suggests that these models may be the ones closest to reality.

All of these computations were completed before the two San Bernardino Mountains earthquakes of June 1922, so the new fault segments which they revealed are not included in our finite element grid. However, the grid does include the Pipes Canyon fault, which is parallel and close to the rupture of the larger event at Landers. Thus, the range of model slip rates that we found for the Pipes Canyon fault (0.2~2.1 mm/year) may be of interest to help place these events in context. Apparently, major events on these faults should have long recurrence times, and the fact that these segments now appear to be more active than the adjacent San Andreas fault is only an artifact of the short instrumental record.

SUMMARY AND CONCLUSION

1. The best are those with fault friction coefficients of 0.17, among models which have no shear tractions on the mantle. The activity of so many faults of diverse trend in California is proof of strong strength contrast between faults and the intervening blocks.

2. Models of this study can approximate the observed variations in the maximum depth of seismicity without resorting to lateral variations in the creep rheology of the lower crust; known variations in heat flow and strain rate are sufficient explanation. The mean temperature of the brittle-ductile transition in San Andreas tectonics, California is the range of 350~410°C.

3. The upper mantle lithosphere of California is converging on a downwelling zone along the Transverse Ranges, and shear tractions from the mantle are necessary in a good model of current tectonics. The magnitude of these tractions is about 8-14 MPa in the Transverse Ranges area, and less elsewhere. The inclusion of mantle drag in these models

does not affect the conclusion that, if all faults have the same friction, that friction is low at 0.25~0.17°C.

4. A theoretical explanation for the weakness of faults involves an up flow of pore water from the mantle or lower crust-perhaps the water subducted during the long Jurassic-Tertiary convergence at the Pacific margin. If such water preferentially rises in faults, then its weakening effect might well be proportional to the thickness of fault gouge, which in turn is proportional to net slip. The best model found was one in which all faults are weak, and the San Andreas is only slightly weaker. However, a model in which new faults are strong and anomalous weakening is slip dependent cannot be strongly rejected.

5. The ranges of fault slip rates predicted by the best models from experiments sets like ours may be useful in long term seismic hazard evaluation, particularly for thrust faults and inaccessible faults of the coastline and borderland.

REFERENCES

Barnhart, J.T. (1973) The Northridge Hills and associated faults: A zone of high seismic probability?, Assoc. Eng. Geol. Spec. Pub., Univ. Publishers, Los Angeles, p. 253-256.

Bird, P. (1978a) Stress and temperature in subduction shear zones: Tonga and Mariana, Geophys. J.R. Astron. Soc., 55, p. 411-434.

Bird, P. (1978b) Initiation of intracontinental subduction in the Himalaya, J. Geophys. Res., 83, p. 4975-4987.

Bird, P. (1984) Hydration phase diagrams and friction of montmorillonite under laboratory and geologic conditions, with implications for shale compaction, slope stability, and strength of fault gouge, Tectonophysics, 107, p. 235-260.

Bird, P. (1989) New finite element techniques for modeling deformation histories of continents with stratified temperature dependent rheology, J. Geophys. Res., 94, p. 3967-3990.

Bird, P., and Baumgardner, J. (1984) Fault friction, regional stress, and crust mantle coupling in southern California from finite element models, J. Geophys. Res., 89, p.1932-1944.

Bird, P., and Rosenstock, R. (1984) Kinematics of present crust and mantle flow in southern California, Geol. Soc. Am. Bull., 95, p. 946-957.

Brace, W.F., and Kohlstedt, D.L. (1980) Limits on lithospheric strength imposed by laboratory experiments, J. Geophys. Res., 85, p. 6248-6252.

Budding, K.E., Schwartz, D.P., and Oppenheimer, D.H. (1991) Slip rate, earthquake recurrence, and seismogenic potential of the Rodgers Creek fault zone, northern California: Initial results, Geophys Res. Lett., 18, p. 447-450.

Byerlee, J. (1990) Friction, overpressure, and fault normal compression, Eos, 71, p. 1580.

Carprette, D.S., Ma, C., and Ryan, J.W. (1992) Crustal Dynamic Project, data analysis-1990, VLBI geodetic results, 1979-1989, NASA Technical Memorandum, TM-100765, Goddard Space Flight Center, Greenbelt, Maryland.

Crowell, J.C., and Sylvester, A.G. (1979) Tectonics of the juncture between the San Andreas fault system and the Salton Trough, Dept. of Geol. Sci., U. of Calif., Santa Barbara.

Cummings, J.C. (1968) The Santa Clara Formation and possible post-Pliocene slip on the San Andreas fault in Central California, Publ. Geol. Sci., 11, Stanford U., Stanford, p. 191-207.

Davis, G.A., and Burchfiel, B.C. (1973) Garlock fault of southern California: An intracontinental transform structure, Geol. Soc. Am. Bull., 84, p. 1407-1422.

DeMets, C., Gordon, R.G., Argus, D.F., and Stein, S. (1990) Current plate motions, Geophys. J. Int., 101, p. 425-478.

De Rito, R.F., Lachenbruch, A.H., Moses, T.H., Jr., and Munroe R.J. (1989) Heat flow and thermotectonic problems of the central Ventura Basin, southern California, J. Geophys. Res., 94, p. 681-699.

Dickinson, W.R. (1972) Test of new global tectonics: Discussion, Am. Assoc. Pet. Geol Bull., 56, p. 375-384.

Dokka, R. K. (1983) Displacements on late Cenozoic strike slip faults of the central Mojave desert, California, Geology, 11, p. 305-308.

Dokka, R.K., and Travis, C.J. (1990a) The Eastern California Shear Zone and its role in the tectonic evolution of the Pacific-North American Transform boundary, Geol. Soc. Am. Abstr. Prog., 22, p. 19.

Ehlert, K.W., and Ehlig, P.L. (1977) The polka-dot granite and the rate of displacement on the San Andreas fault in southern California, Geol. Soc. Am. Abstr. Prog., 9, p. 415-416.

Graham, S.A., and Dickinson, W.R. (1978) Apparent offsets of on-land geologic features across the San Gregorio-Hosgri Fault trend, Calif. Div. Mines Geol. Spec. Rep., 137, p. 13-23.

Hamilton, D.H., and Willingham, C.R. (1977) Hosgrio fault zone: structure, amount of displacement, and relationship to structures of the western Transverse Ranges, Geol. Soc. Am. Abstr. Prog., 9, p. 429.

Han, U. (1991) An Analytical Model Study on the Thermal Stress around the Uplifted Province within the Continental Lithosphere, J. Korean Inst. Mining Geol., 24, p. 57-62.

Han, U., and Keehm, Y. (1997) Thermal Stress Distribution within the Lithosphere of East Sea of Korea, J. Korean Earth Sci. Soc., 18, p. 176-182.

Harden, J.W., and Matti, J.C. (1989) Holocene and late Pleistocene slip rates onthe San Andreas fault in Yucaipa, California, Geolo. Soc. Am. Bull., 101, p. 1107-1117.

Henyey, T.L. (1968) Heat flow near major strike slip faults in central and southern California, Ph,D, thesis, Cal. Inst. of Tech., Pasadena, p. 415.

Henyey, T.L., and Wasserburg, G.T. (1971) Heat flow along

major strike slip faults in California, J. Geophys. Res., 76, p. 7924-7946.
Hickman, S.H., Younker, L.W., Zoback, M.D., and Cooper, G.A. (1995) The San Andreas fault zone drilling project, J. Energy Resour. Technol., 117, p. 263-270.
Hubbert, M.K., and Rubey, W.W. (1959) Role of fluid pressure in the mechanics of overthrust faulting, Geol. Soc. Soc. Am. Bull., 70, p. 115-206.
Kennedy, M.P. (1975) Geology of the San Diego metropolitan area, Califprnia, Calif. Div. Mines Geol. Bull., 200, p. 1-39.
Kirby, S.H. (1983) Rheology of the lithosphere, Rev. Geophys. Space Phys., 21, p. 1458-1487.
Lachenbruch, A.H., and Sass, J. H. (1980) Heat flow and energetics of the San Andreas fault zone, J. Geophys. Res., 85, p. 6185-6222.
Lamar, D.L. (1961) Structural evolution of the northern margin of the Los Angeles basin, Ph.D. thesis, U. Calif. Los Angeles.
Lisowski, M., Savage, J.C., and Prescott, W.H. (1991) The velocity field along the San Andreas fault in central and southern California, J. Geophys. Res., 96, p. 8369-8389.
Mansinha, L., and Smylie, D.E. (1971) The displacement fields of inclined faults, Bull. Seismol. Soc. Am., 61, p. 1443-1450.
Mooney, W.D., and Weaver, C.S. (1989) Regional crustal structure and tectonics of the Pacific coastal states; California, Oregon, and Washington, in: L.C. Pakiser and W.D. Mooney (Ed.), Geophysical Framework of the Continental United States, Geol. Soc. Am. Mem., 172, p. 129-161.
Morton, D.M., Matti, J.C., Miller, F.K., and Reppening, C.A. (1986) Constraints on strike slip displacements on the San Andreas and San Jacinto faults, Geol. Soc. Am. Abstr. Prog., 18, p. 161.
Mount, V.S., and Suppe, J. (1987) State of stress near the San Andreas fault: Implications for wrench tectonics, Geology, 15, p. 1143-1146.
Pinter, N., and Sorlien, C. (1991) Evidence of latest Pleistocene to Holocene movement on the Santa Cruz Island fault, California, Geology, 19, p. 909-912.
Prentice, C.S. (1989) Earthquake geology of the northern San Andreas fault near Point Arena, California, Ph.D. thesis, Cal. Inst. Tech., Pasadena, p. 252.
Prentice, C.S., Weldon, R.J., and Sieh, K.E. (1986) Distribution of slip between the San Andreas and San Jacinto faults near San Bernardino, California, Geol. Soc. Am. Abstr. Prog., 18, p. 172.
Rice, J.R. (1990) Fault stress states, pore pressure distributions, and weakness of the San Andreas fault, Eos, 71, p. 1652.
Sanders, C.O. (1990) Earthquake depths and the relation to strain accumulation and stress near strike slip faults in southern California, J. Geophys. Res., 95, p. 4751-4762.
Sarna-Wojcicki, A.M. (1986) Displacement of a circa 6M a tuff across the San Andreas fault system, northern California, EOS, 67, p. 1224.
Sass, J.H. (1997) Thermal regime of the San Andreas fault near Parkfield, California, J. Geophys. Res., 102, p. 27575-27585.
Savage, J.C., Lisowski, M., and Prescott, W.H. (1990) An apparent shear zone trending North-northwest across the Mojave Desert into Owens Valley, eastern California, Geophys. Res. Lett., 17, p. 2113-2116.
Segall, P., and Davis, J.L. (1997) GPS applications for geodynamics and earthquake studies, Annual Reviews of Earth and Planetary Science, 25, p. 301-336.
Segall, P., and Freymueller J. (1995) Kinematics of the Pacific-North America Plate Boundary Zone, N. California, Stanford Univ.
Sharp, R.V. (1967) San Jacinto fault zone in the Peninsular Ranges of Southern California, Geol. Soc. Am. Bull., 78, p. 705-730.
Turcotte, D.L. (1980) A steady state model for the distribution of stress and temperature on the San Andreas Fault, J. Geophys. Res., 85, p. 6223-6230.
Ward, P.L., and Page, R.A. (1989) The Loma Prieta earthquake of October 17, 1989, U.S. Geol. Surv. Pamphlet, U.S. Gov. Print. Off., p. 16.
Weldon, R., and Humphreys, E. (1986) A kinematic model of southern California, Tectonics 5, p. 33-48.
Wesnousky, S.G., Prentice, C.S., and Sieh, K.E. (1991) An offset Holocene stream channel and the rate of slip along the northern reach of the San Jacinto fault zone, San Bernardino Valley, California, Geol. Soc. Am. Bull., 103, p. 700-709.
Williams, C.F. (1995) Temperature and the seismic/aseismic transition, Eos Trans. AGU, 76, Fall.
Yeats, R.S. (1973) Newport-Inglewood fault zone, Los Angeles basin, California, Am. Assoc. Pet. Geol. Bull., 57, p. 117-135.
Yeats, R.S., and Huftile, G.J. (1990) Convergence rates across w. Transverse Ranges, U.S. Geol. Surv. Open-File Rep., 90-680, p. 171-173.
Zhang, P., Ellis, M., Slemmons, D.B., and Mao, F. (1990) Right-lateral displacements and the Holocene slip rate associated with prehistoric earthquakes along the southern Panamint Valley fault zone: Implications for southern Basin and Range tectonics and coastal California deformation, J. Geophys. Res., 95, p. 4857-4872.
Zoback, M.D. (1987) New evidence on the state of stress of the San Andreas fault system, Science 238, p. 1105-1111.
Zoback, M.L., and Zoback, M.D. (1989) Tectonic stress field of the continental United States, in: L.C. Pakiser and W.D. Mooney (Ed.), Geophysical Framework of the Continental United States, Geol. Soc. Am. Mem., 172, p. 523-539.

1999년 3월 30일 원고접수, 2000년 1월 10일 게재승인.

낮은 강도를 갖는 주요 단층의 slip movement에 대한 시뮬레이션

박무춘* · 한 욱*

요 약 : 본 논문은 고도, 지열류량, 지진, 측지 자료, 지각 두께와 년 1 mm이상의 이동율을 갖는 산안드리아 지역에서 주요 단층운동을 모델화하기 위하여 얇은 지판에서의 변화를 유한요소법을 이용하여 단층의 네트웍을 시뮬레이션함으로써 실제 관측 결과와 비교하였다. 판에 있어서 속도의 경계 조건은 NUVEL-1판 모델과 Great Basin에서의 지각 변형량을 기초로 하였다. 지각의 마찰과 전위포행 상수들은 350~410°C에서 발생될 수 있는 지진의 최대 깊이에서 관측된 변화 정도를 도출하기 위해서 계산되었다. 유동학적 상수들은 단층면에서의 마찰계수와 하부지각에서의 발생 가능한 반응에너지에 한정하였다. 이러한 두가지 변수는 3가지 실험 모델에서 체계적으로 변화되는 경향을 나타낸다. 모델의 변화 양상은 주요 단층에 대한 마찰율이 0.17~0.25의 값을 가질 경우에 가장 적합하다. 또한 단층의 약한 성질은 순수한 slip량과 일치하거나 비례하는 경향을 보인다. 지질학적인 자료 분석 결과는 단층의 약한 성질이 이동에 종속적이며 30% 범위내에서 변화를 나타내고 있음을 보여준다. 최적의 모델은 년 3 mm이하의 오차를 보이는 자료의 경우에 가장 잘 설명될 수 있으며, 더욱이 자료가 전무한 지역에서도 지진재해와 그 활동성 예측이 가능하다.